communications physics

Article

https://doi.org/10.1038/s42005-025-01939-z

Unveiling the complex morphologies of sessile droplets on heterogeneous surfaces

Yanchen Wu [1,2,4,5], Hongmin Zhang [1,2,5], Fei Wang [1,2] ✉ & Britta Nestler [1,2,3]

Droplets exhibiting a myriad of shapes on surfaces are ubiquitous in both nature and industrial applications. In high-resolution manufacturing processes, e.g., semiconductor chips, precise control over wetting shapes is crucial for production accuracy. Despite the high demand for describing droplet wetting shapes and their transformations across a wide range of applications, a robust model for precisely depicting complex three-dimensional (3D) wetting droplet shapes on heterogeneous surfaces remains elusive. Herein, we fill this gap by developing a universal, high-precision model that accurately describes wetting shapes, including those with polygonal baselines and irregular footprints. Our model reveals the intricate wetting morphologies beyond the classic Young's law and Cassie-Baxter-Wenzel models. Besides, it aligns quantitatively with physical simulations for various droplet volumes. This work provides a potential method to achieve highly complex morphologies of droplets via low-cost beforehand design of the surfaces, thereby opening up potential applications in 3D printing, printed electronics, and microfluidics.

On a homogeneous solid substrate, the droplet forms a spherical cap, which can be fully described by the classic Young's equation[1]. However, real-life surfaces are often heterogeneous with varying physical and/or chemical properties. In this case, the droplet behavior becomes much more complex than Young's consideration. The heterogeneous surfaces usually lead to contact angle hysteresis effect[2–7] as well as anisotropic wetting phenomena[8,9]. In this complex real-life scenario, traditional models like Young's law or Cassie-Baxter-Wenzel model[10–12] often fail to accurately describe the anisotropic droplet shapes[13–15]. In this work, we will shed light on the knotty issue of equilibrium droplet shapes on heterogeneous surfaces by proposing an alternative concept, namely the contour curve method. The current concept is expected to be able to cope with highly irregular footprints of droplets in real-life applications.

Droplet manipulation on heterogeneous surfaces has sparked great interest in bio-mimetic studies[16–18], surface science[19,20], heat management researches[21–23], fabrication of functional artificial structures[24–26], self-assembly of ordered structures in photonics[27], cryopreservation of food emulsions[28], drug delivery systems[29,30], microreactors and microfluidics[31–34], to name a few. Through an elaborate design of the heterogeneity on the solid surfaces, the droplet shape can be accurately tailor-made[35–37]. For instance, the heterogeneity of the surface can be manipulated through a combination of nano-/micro-structure and surface chemistry[38,39]. Despite the high significance of precisely controlling droplet shapes, previous treatments regarding a full description of complex 3D wetting droplets remain rudimentary; previous studies often rely on geometrical assumptions, image processing, spline fitting, or numerical integration[40–42]. These approaches oversimplify the intricate nature of droplet behavior and cannot accurately depict the full details of droplet shapes. Therefore, there is a significant need for developing a robust method that can elaborately capture the behavior of droplets on heterogeneous surfaces, especially, when the heterogeneity is highly irregular.

In this work, inspired by the phenomena of the Newton ring effect (Fig. 1a, b[43]) and the Suminagashi pattern of Japanese art (Fig. 1c, d[44–46]), we will propose a contour curve method to address complex 3D shapes of droplets on specifically designed patterned surfaces; see schematics for droplets on polygon and irregular patterns in Fig. 1e–h), respectively. Our method is capable of precisely describing the equilibrium shape of a droplet when the volume and the base shape are arbitrarily given. In addition, the current method will provide a simple solution for measuring the volume of a droplet *posteaquam* depositing on a solid surface, which is significantly challenging in experiments because of the rapid evaporation and the existence of irregular droplet-footprint. We will demonstrate the feasibility of

[1]Institute of Nanotechnology, Karlsruhe Institute of Technology, Hermann-von-Helmholtz Pl. 1, Eggenstein-Leopoldshafen, 76344, Germany. [2]Institute of Applied Materials, Karlsruhe Institute of Technology, Straße am Forum 7, Karlsruhe, 76131, Germany. [3]Institute of Digital Materials Science, Karlsruhe University of Applied Sciences, Moltkestraße 30, Karlsruhe, 76133, Germany. [4]Present address: Department of Chemical Engineering, Massachusetts Institute of Technology, 77 Massachusetts Avenue, Cambridge, MA, 02139, USA. [5]These authors contributed equally: Yanchen Wu, Hongmin Zhang. ✉e-mail: fei.wang@kit.edu

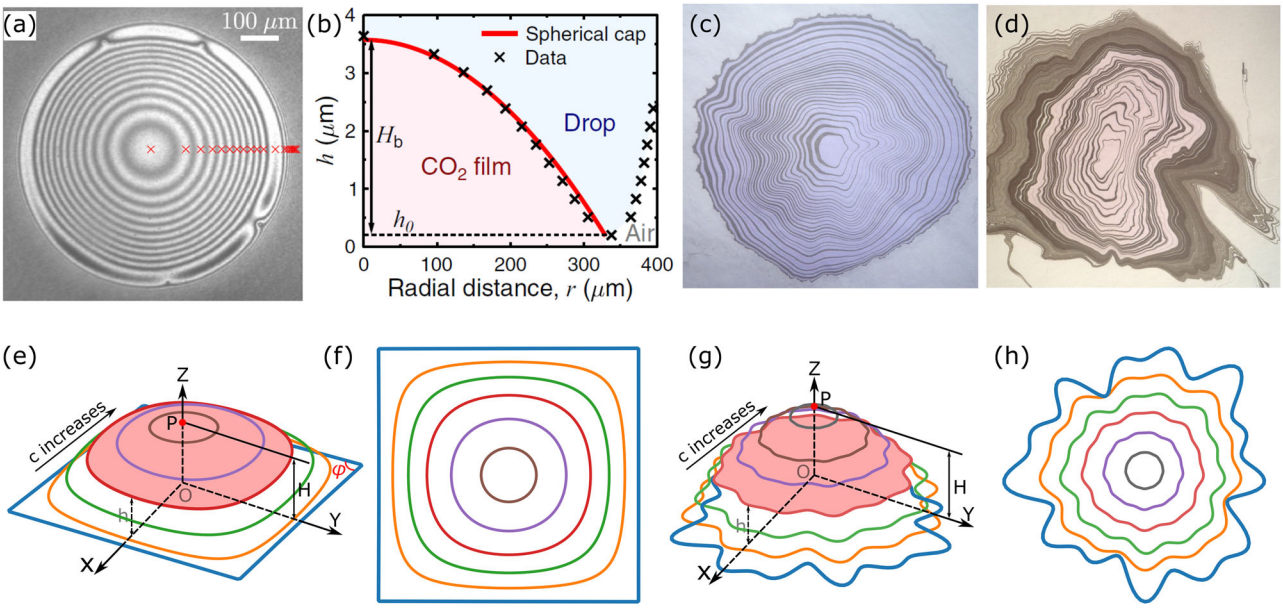

Fig. 1 | Morphologies of sessile droplets. a Bottom view of contact region between the drop and the substrate via reflection interference contrast microscopy. The bright Newton rings are highlighted with red crosses and show the change of one half of the wavelength of light as the thickness of the gas film changes from the center to the edge of the contact region. **b** The gas film height h as a function of radial distance r. The liquid-gas interface forms a nearly spherical cap (red solid line) with a maximum height H_b placed on a film with a height h_0. Experimental results reproduced from Ref. 43, used under CC BY 4.0. Modified from the original. **c**, **d** Pictures for Suminagashi pattern of ink on a water surface created by Bea Mahan[46], used under CC BY-NC-ND 2.0. **e** An equilibrium droplet shape on a square-patterned substrate is described by a series of contour curves with varying c (see Eq. (2)) in $OXYZ$ coordinate system. The red point P highlights the apex of the droplet and H depicts the droplet height. The angle φ indicates the interior angle of the base pattern. **f** Top view of the schematic droplet in (**e**). **g** An equilibrium droplet shape on an irregular-patterned substrate is described by a series of contour curves with varying c in $OXYZ$ coordinate system. **h** Top view of the schematic droplet in (**g**).

correlating the volume of the equilibrated droplet, irrespective of its shape, to its height; this implies that the droplet volume can be ascertained simply by detecting its height. Moreover, we will establish a universal functional relationship between the surface area of the distorted droplet cap and the droplet height. This method, which is shape-agnostic, has the potential to offer efficiency benefits over conventionally applied optical methods, such as interferometric imaging[47] and lensing technique[48]. For instance, Zhang et al.[49] utilized confocal microscopy to monitor the lateral diameter and to measure contact angles of nanodroplets, achieving high spatial resolution with an uncertainty of 70 nm. Unlike the determination of droplet morphology through the color of Newton-rings, the present contour curve method can be much denser than the Newton rings, so that the precision can be significantly increased. However, the current approach may not achieve high precision on the scale of several nanometers where the fluctuations become significant. Similar to the Surface Evolver method[50], the contour curve method is also based on minimizing the total free-energy with a constrained volume. Surface Evolver is within the framework of sharp interface, where the interface is discretized by a mesh of triangles. The surface tension force exerting on each vertex of the triangulation drives the mesh to a minimal energy configuration. It does not involve any geometrical simplification, allowing for an accurate description of droplet shapes with curved contact lines. Compared to the Surface Evolver method, the present contour curvature method is much simpler to implement and can be applied to a wide range of droplet shapes without the need for complex computational resources. This makes it accessible for preliminary analyses and advantageous in experimental setups where quick assessments are needed. However, it may lack the precision for more sophisticated cases, particularly when dealing with 3D surface structures that are comparable with the size of the droplet.

Results

We describe the total surface energy E of the droplet as

$$E = \sigma S + \gamma_1 S_1 + \gamma_2 S_2, \tag{1}$$

where σ, γ_1, and γ_2 depict the interfacial tensions of liquid-gas, solid-liquid, and solid-gas interfaces, respectively; S, S_1, and S_2 represent the total surface areas of liquid-gas, solid-liquid, and solid-gas, respectively. On a homogeneous surface, the minimization of E subjected to a constant volume leads to the Young's law and the Young's contact angle θ_Y; the droplet cap has a uniform mean curvature resulting from the Young-Laplace pressure. On a heterogeneous surface consisting of a polygon-superhydrophilic island embedded in a superhydrophobic matrix, the droplet base is confined within the polygon-island; this scenario is often observed in the cell culture process for high-throughput assays and micro-droplet reactions[51–54]. As in the case of homogeneous surfaces, the droplet cap also forms a mean curvature surface with a local contact angle θ_Y varying along the perimeter of the droplet base. For brevity and without loss of generality, we consider polygon islands with a constant surface area and set $\sigma = 1$ as a reference value. In such a consideration, the total surface energy is rewritten as $E = \sigma S + E_0$, where $E_0 = \gamma_1 S_1 + \gamma_2 S_2$ is a constant. The problem is then reduced to the minimization of the surface area of the droplet cap S subjected to a constant droplet volume.

Drawing parallels to the concept of curve shortening flow and Gage-Hamilton-Grayson theorem[55,56], we characterize the liquid-gas interface by using a series of contour curves. These contour curves are obtained by slicing the droplet cap at various heights h parallel to the droplet base, as depicted in Fig. 1e–h). There are two central constraints for the contour curves. (I) At the droplet base ($h = 0$), the curve manifests as a polygon or a specified irregular pattern (e.g., the blue square in Fig. 1e, f) and the blue irregular pattern in Fig. 1g, h). (II) As h increases, these curves progressively smooth out, approximating a circular shape near the droplet apex P and eventually converging to the singular point P. This is akin to the mechanism of curve shortening flow, albeit with distinct shortening kinetics.

Polygon patterns

To fulfill the constraints (I) and (II) for a droplet on a polygonal pattern, we construct the following mathematical formulation to depict the contour

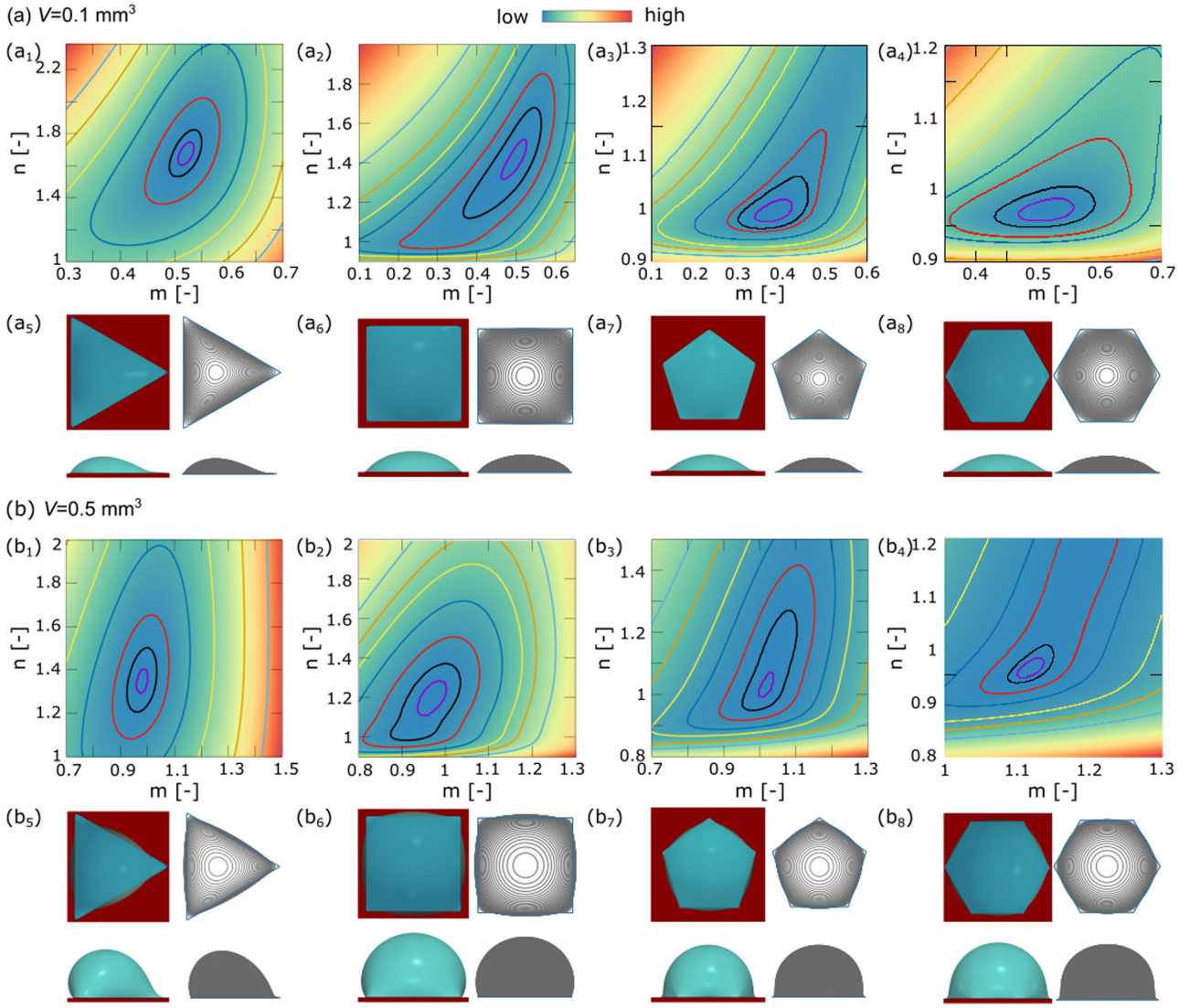

Fig. 2 | Morphological diagram for equilibrium droplets on four representative polygon patterns. The liquid-solid contact area S_1 = 1 mm^2 is kept constant. **a** V = 0.1 mm^3, **b** V = 0.5 mm^3. (a_1)-(a_4) and (b_1)-(b_4) describe the heat maps for the surface area of the droplet cap, $S(m, n)$. The contour lines indicate the surface area levels and the color changes from red to blue, indicating the decrease of the surface area S. The snapshots beneath the corresponding heat maps (a_5)-(a_8) and (b_5)-(b_8) illustrate the top and side views of the equilibrated droplets via phase-field simulations (green colored droplet with red substrate) and contour curve method (gray-colored droplet).

curves in the OXY coordination system as

$$(-1)^N \prod_{i=1}^{N} \left\{ \frac{1}{Rf(c)} \left[y \sin(i\varphi) + x \cos(i\varphi) \right] - 1 \right\} - c = 0. \qquad (2)$$

Here, N represents the number of the sides of the polygon ($N \geq 3$) and R stands for the radius of the inner tangent circle of the polygon. The index i ($i = 1, 2, \ldots, N$) depicts the i-th side of the polygon. For instance, a 1 × 1 mm^2 square pattern corresponds to $N = 4$ and $R = 0.5$ mm. Note that the contour curves at different heights h have distinct perimeter and roundness (Fig. 1f, h). The variation of the perimeter and the roundness of the contour curves is achieved by introducing two simple controlling functions: $f(c) = (1 + c)^m$ and $h(c) = Hc^n$. The variable c varying from 0 to 1 governs the roundness of the contour curve and the constant H represents the height of the droplet apex. Given a specific droplet volume V and base pattern, the surface area of the droplet cap S is solely a function of the power factors m and n. The physical meaning of the power factors m and n is the variation of the short-range interaction of liquid-gas-solid with h. Therefore, the equilibrium state of the droplet is determined by addressing the minimum of the heat map, $S(m, n)$ (Fig. 2). For an in-depth understanding of the contour curve method, readers are referred to Supplementary Note 1 and 2.

To further confirm the droplet morphologies from the contour curve method, we employ the well-established phase-field model[57] to simulate the equilibrium droplets on the patterned surfaces. This model has proven its efficacy in accurately representing wetting phenomena on homogeneous surfaces, chemically patterned substrates, and mechanically structured surfaces[14,58,59]. In the phase-field simulations, we set the Young's contact angles θ_Y on hydrophilic and hydrophobic regions as 0° and 180°, respectively. This allows the droplets to be perfectly confined within the hydrophilic islands, as considered in the high-throughput assays for cell culturing[51,60]. By minimizing the Ginzburg-Landau free energy of the system, the equilibrium states of droplets are achieved in the numerical simulations.

Next, we employ both phase-field and contour curve methods to explore the 3D equilibrium morphologies of the droplets. We examine droplets with volumes ranging from 0.1 mm^3 to 1.5 mm^3, which are released on the specifically designed hydrophilic patterns with a fixed area of 1 mm^2. Driven by the capillary force, these droplets reach the

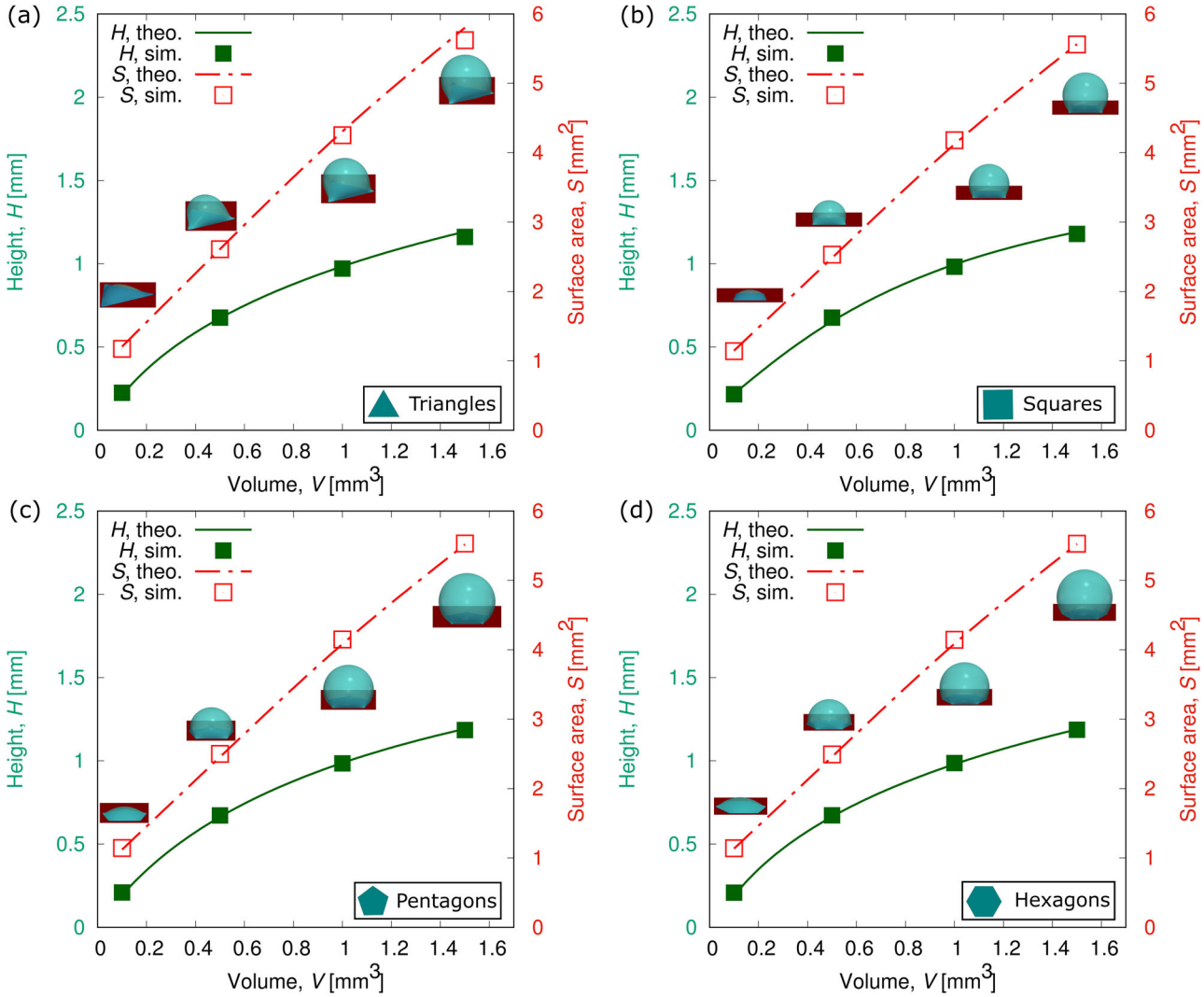

Fig. 3 | Surface area of the droplet cap S and the droplet height H as a function of volume V for the four representative polygon patterns. a–d display the results for triangles, squares, pentagons, and hexagons patterns, respectively. The inset snapshots show a high angle view of the equilibrated droplets via phase-field simulations.

equilibrium states at the end. Figure 2 illustrates the equilibrium morphologies of the droplets on four representative polygon patterns, namely, triangles, squares, pentagons, and hexagon patterns. As an example, we show the results for two representative volumes, $V = 0.1\ \text{mm}^3$ (Fig. 2a) and $V = 0.5\ \text{mm}^3$ (Fig. 2b). The heat maps of $S(m, n)$ on the four different polygon patterns are presented in the first rows of Fig. 2a, b). In these heat maps, each contour line indicates the same value of the surface area S. The value of S declines from the red region to the blue region; a minimum value S_{min} can be identified for a certain combination of m and n, which corresponds to the equilibrium state of the droplet. After the determination of m and n in the heat map, the 3D droplet shape is reproduced by using the contour curve method described by Eq. (2). Beneath each heat map, we illustrate the corresponding top and side views of the droplet snapshots obtained from phase-field simulations (green-colored droplet with red substrate) and contour curve method (gray-colored droplet). Both the top and side views show excellent consistency between the contour curve method and numerical simulations.

Figure 3 shows the droplet height H and the surface area of the droplet cap S as a function of droplet volume from the contour curve method (lines) and simulations results (symbols). Figure 3a–d depict the cases for triangles, squares, pentagons, and hexagon patterns, respectively. The inset snapshots show the high angle view of the equilibrated droplets for the corresponding volumes. Excellent agreements between the predictions via the contour curve method and simulation results are observed for all four patterned substrates.

The above discussion is based on the assumption that the droplet is perfectly confined within the predefined superhydrophilic polygon island. Thus the liquid-solid contact area S_1 is constant. However, if the contact angle hysteresis is significant, the droplet may not be fully confined within the hydrophilic area. In this scenario, the liquid-solid contact area S_1 is no more constant and depends on the advancing contact angle. In such cases, the droplet's base profile and 3D shape can be accurately determined through numerical simulations, such as phase-field or Surface Evolver simulations. This situation has been investigated in ref. 61, where we explored how to use real chemically patterned surfaces to manipulate the shapes of inkjet-printed droplets according to the associated contact angle hysteresis at the chemical interface of hydrophilic and hydrophobic areas.

In what follows, we incorporate the effect of the contact angle hysteresis, specially, the advancing contact angle, in the current contour curve method. To approximate the equilibrium shape of a droplet ($V = 0.5\ \text{mm}^3$) on a hydrophilic square ($1\ \text{mm}^2$) patterned surface with different advancing contact angles on the hydrophobic part of the surface, we use the contour line function, $(y/R_0 - 1)(y/R_0 + 1)(x/R_0 - 1)(x/R_0 + 1) - c_0 = 0$ with given values of the geometry parameters (R_0, c_0) to denote the droplet blase lines, as displayed in Fig. 4a. By rescaling the range of c from [0, 1] to $[c_0, 1]$, we reformulate $f(c)$ and $h(c)$ as $f(c) = (1 + \frac{c-c_0}{1-c_0})^m$ and $h(c) = H(\frac{c-c_0}{1-c_0})^n$.

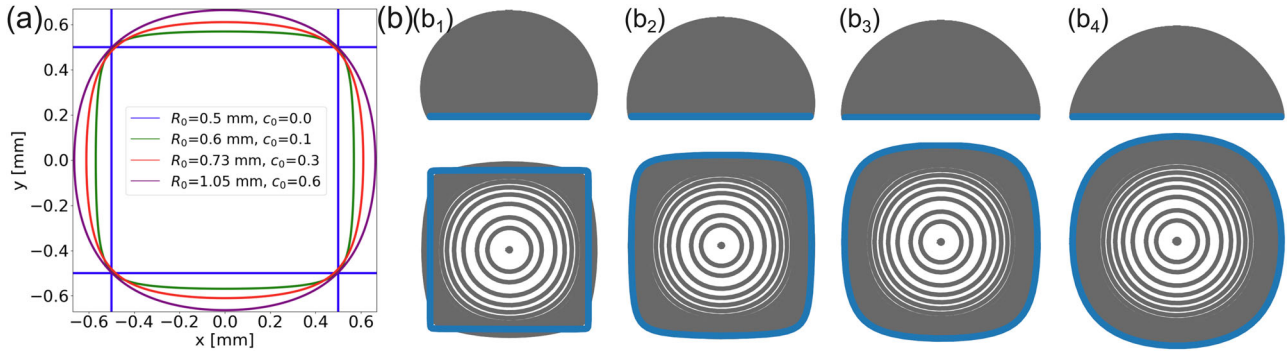

Fig. 4 | Morphological diagram using the contour curve method for equilibrium droplets on a square pattern with different advancing contact angles. a The base lines of the droplets are depicted by $(y/R_0-1)(y/R_0+1)(x/R_0-1)(x/R_0+1)-c_0=0$ with given values of (R_0, c_0), which correspond to different advancing contact angles on the hydrophobic part of the surface (see Table 1). **b** Side and top views of the droplets with different advancing contact angles. The droplet base lines are highlighted in blue. Here, we keep the volume of the droplets $V = 0.5\ \text{mm}^3$ constant and show the results for droplets with different base lines (from (b_1) to (b_4), we choose (R_0, c_0) according to image (a)).

Table 1 | Geometry parameters of droplets on a square patterned substrate as shown in Fig. 4

Parameters	Values			
$(R_0(\text{mm}), c_0)$	(0.5, 0)	(0.6, 0.1)	(0.73, 0.3)	(1.05, 0.6)
$\theta_a(^\circ)$	105	91	79	56
$H(\text{mm})$	0.66	0.61	0.60	0.56
$S_1(\text{mm}^2)$	1.00	1.22	1.32	1.47
$S(\text{mm}^2)$	2.49	2.45	2.43	2.44

The droplet volume $V = 0.5\ \text{mm}^3$ is constant.

Thereafter, we adopt the contour curve method to calculate the 3D shapes of the droplets. The results of the side and top views are demonstrated in Fig. 4b, where the droplet base lines are highlighted in blue color. We list the calculated geometry parameters of these droplets in Table 1. The advancing contact angle θ_a is obtained by measuring the side view profile, which is also the largest local contact angle of the droplet. We find that as the droplet base line extends outward and gradually approaches a circle (from (b_1) to (b_4) in Fig. 4b), the liquid-solid contact surface increases, while both the advancing contact angle θ_a and droplet height H decrease. The liquid-gas interface area decreases and then increases, due to the competing effect between the interface distortion caused by the patterned surface and the wettability of the substrate. Note that a significant advantage of the contour curve method over PF simulations is that it allows one to analyze the 3D shapes of droplets on patterned surfaces with contact angle hysteresis effect without knowing the details of advancing/receding contact angles. This can be beneficial in experimental setups, where quick assessments of droplet shapes are needed, but only top or bottom views of the droplet are accessible. Vice versa, one can also use the experimentally measured advancing contact angle as an input to predict the base line via solving the unknowns R_0 and c_0. We will discuss more details about droplets with rough contact lines in the following sections, which are related to contact angle hysteresis effect.

Flower patterns

We further extend the contour curve method to describe 3D droplet shapes with an arbitrary footprint by adjusting the formulation of the contour curves as

$$r = \frac{1}{f(c)}(1-c)^p R_0 + (1-c)^q R_b, \tag{3}$$

where r is the radial distance in the polar coordinate; R_0 is a constant associated with the area of the droplet base, and R_b represents a perturbation term related to the shape of the droplet. The indexes p and q govern the evolution of the size and the shape of the contour lines as the variable c varies from 0 to 1. By following the same strategy as handling the droplets on polygon-patterned substrates, we identify the minimum surface area S_{min} through the heat map $S(m, n)$ and determine the corresponding values of m and n. This allows us to uniquely determine the 3D droplet shape at equilibrium.

As a typical example for droplets on irregularly patterned substrate (also referred to as flower patterned substrate in the following), we set $R_0 = 0.561\ \text{mm}$ and $R_b = A[\cos(3\theta) + \cos(8\theta) + \sin(13\theta)]$. Here, the amplitude A is set as 0.05 mm and θ denotes the polar angle in the polar coordinate. The droplet base area is $1\ \text{mm}^2$. To align with the contour line evolution with height, we set the indexes $p = 0.5$ and $q = 4$. In Fig. 5a, we show the droplet height H and the surface area S versus volume V from both the contour curve method (lines) and simulations (symbols). In Fig. 5b, c, we display the heat map $S(m, n)$ of a $0.1\ \text{mm}^3$ droplet on the irregularly patterned surface as well as the comparison of the top and side views of the equilibrated droplets. In Fig. 5d, e, we show the case for a droplet of the volume $0.5\ \text{mm}^3$. Overall, we observe a good agreement between the contour curve method and the phase-field simulations. This demonstrates the justification and robustness of the proposed contour curve method for describing 3D shapes of a droplet with an arbitrarily shaped footprint.

To make it easier for readers to understand the contour curve method and its parametric setup, we list the key parameters of the model in Tab. S1 (see Supplementary Note 3). We emphasize that the contour curve model is based on an assumption that the droplet base line is known and the liquid-gas interface is described with a series of contour curves, which are delicately stacked in three dimensions to achieve a surface energy minimum state. Given the flexibility of the chosen geometrical constrain functions, such as $f(c)$ and $h(c)$ and the power factors (p, q, m, and n) in the formulations of contour curves, this model provides an efficient approximation of the real droplet shapes; minor deviations from the exact solution may occur. This model is more accurate when the geometric parameters and functions can be precisely identified in the energy minimization procedure. In addition, it may not achieve a high level of precision for extremely thin film systems on the scale of several nanometers, where the fluctuations and vibrational noise play a non-neglected role[62]. Our model is limited to the case where surface tension forces are much more important than the gravitational force, i.e., the Bond number is much less than 1. When gravity is pronounced, such as with increased droplet volume, we refer to the ellipsoidal and pancake models[63].

Geometric properties of sessile droplets

We further apply the contour curve method to reveal the geometric properties of the 3D droplets on surfaces of flower pattern, polygon patterns with $N = 3, 4, 5, 6$, and circular pattern. Figure 6a, b, c illustrate the droplet height

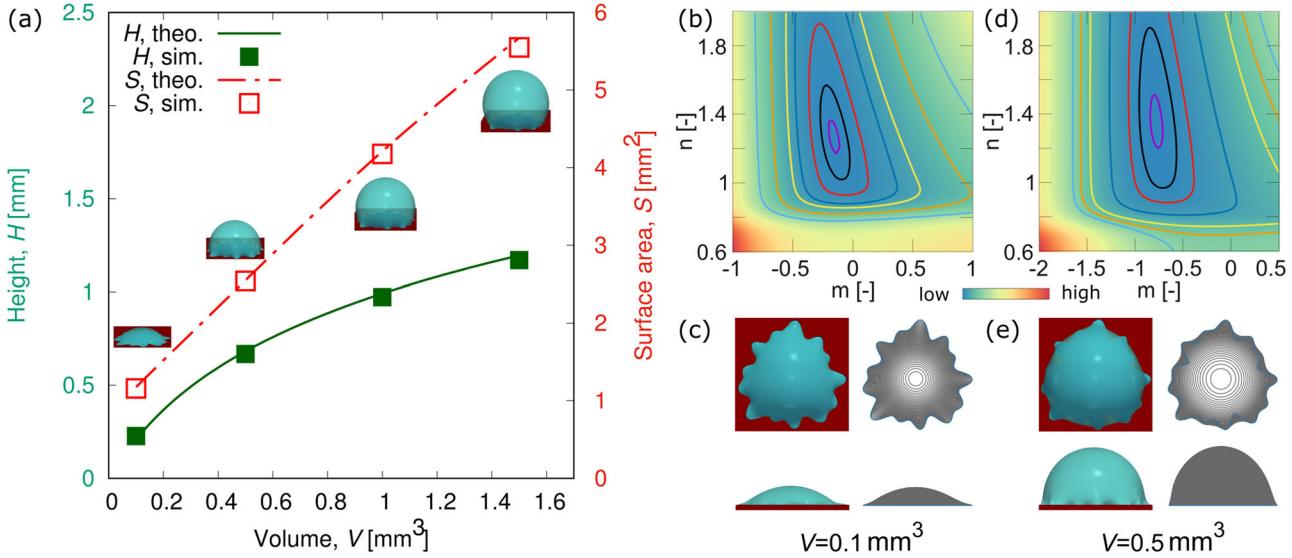

Fig. 5 | Droplet morphologies on a flower-shape patterned surface. a Surface area of the droplet cap S and the droplet height H as a function of the droplet volume V. Heat maps for $S(m, n)$ for two different volumes ((**b**): $V = 0.1$ mm^3; (**d**): 0.5 mm^3). **c**, **e** Snapshots for the top and side views of the equilibrated droplets via phase-field simulations and contour curve method ((**c**): $V = 0.1$ mm^3; (**e**): 0.5 mm^3).

H versus the volume V, the surface area versus the volume V, and the surface area S versus the droplet height H, respectively (flower and polygon patterns: symbols; circular pattern: dot dashed lines). The insets zoom in on specific parts of the corresponding plots and highlight the differences in the results for different patterns. Two key observations are summarized as follows. (I) As N increases from 3 to 6, the results for the polygon patterns monotonically approach the one for the circular pattern. This is due to the fact that a larger N gives rise to a relatively smaller disparity between the irregular droplet caps and the spherical cap. (II) The curves for the flower pattern lie between the ones of the triangle and square patterns. This observation indicates an intermediate distortion of the droplet cap, contrasting to a stronger distortion on the triangle pattern and a weaker distortion on the square pattern.

To quantify the deviation of the droplet shape from a spherical cap, we introduce a distortion coefficient ξ and propose the following equation to estimate the surface area of the droplet cap

$$S = \xi(S_1 + \pi H^2). \tag{4}$$

For the circular pattern, we have $\xi = 1$. The distortion coefficient ξ for each patterned surface is determined by the ratio of the surface area of the droplet cap S to the surface area of a spherical cap having the same volume and the identical base area as the concerned droplet cap. To confirm our hypothesis in Eq. (4), we plot the scaled surface area of the droplet cap S/ξ with the droplet height H in Fig. 6d. It is observed that all the data points collapse onto a single master curve, $S/\xi = S_1 + \pi H^2$; the distortion coefficients ξ for different patterns are listed in the caption of Fig. 6.

As a further application, we adjust the irregularity of the flower pattern to maneuver the equilibrium shapes of the droplets, by which the droplet height and surface area of the droplet cap are precisely regulated. The base area of the droplet is fixed to be 1 mm^2 with $R_0 = 0.561$ mm. To control the footprints of the droplets, we set $R_b = A\cos(N\theta)$. This approach allows us to fine-tune the droplet shapes by varying the parameter N and the amplitude A.

Figure 7 depicts the morphological properties of a droplet with $V = 0.1$ mm^3 on a series of modified flower patterns. In Fig. 7a, we set the amplitude parameter A as a constant ($A = 0.05$ mm) and plot the droplet height H and the surface area S as a function of N. Both H and S increase with N. The corresponding top and side views of the droplets are listed in Fig. 7b. As N increases, there are more and more concave and convex regions of the contact line. The undulated contact line enlarges the surface area of the droplet cap. In Fig. 7c, we keep the parameter $N = 4$ constant and plot H and S vs. A. Figure 7d provides the corresponding top and side views of the droplets on patterns with different A. As A increases, the base line of the droplet becomes more and more distorted, leading to an increase in S. As the distortion of the droplet base line increases, the side view of the droplets changes from a circular arc to a hyperbolic secant.

In line with the distortion and scaling analysis in Fig. 6d, we apply Eq. (4) to describe the function relationship between S and H. We calculate the distortion coefficients ξ for the eight different droplet shapes discussed in Fig. 7, as listed in Table 2. For a fixed value of $A = 0.05$ mm, the distortion coefficient ξ increases with N monotonically, indicating that the perturbation wavelength of the droplet base effectively controls the distortion of the droplet. For a fixed value of $N = 4$, a large ξ is achieved by increasing the amplitude parameter A. For a relatively small A, the droplet shape approaches a spherical cap with $\xi = 1.001$. As A increases from 0.01 mm to 1.15 mm, ξ increases from 1.001 to 1.058. These quantitative studies on the droplet morphologies demonstrate again that a dedicated control of the droplet shapes can be realized by designing the substrate patterns with arbitrary footprints.

Contact angle hysteresis effect

It should be noted, that in principle, it is possible to include the contact angle hysteresis in the current contour curve model by constructing a formulation of the droplet baseline as a function of the advancing and receding contact angles. For instance, for an arbitrary droplet baseline described by Fourier series $\eta(x) = \frac{1}{2\pi}\int_{-\infty}^{+\infty}\tilde{\eta}(Q)e^{iQx}dQ$ with $Q = 2\pi/\lambda$ (λ is the wavelength), the coefficients in the Fourier series are not independent and constrained by the advancing and receding contact angles. However, an exact solution requires solving the Laplace equation together with the wetting boundary condition, which is generally very complex and typically requires numerical methods[64]. To demonstrate the accuracy and robustness of the contour curve method for addressing an arbitrary droplet baseline described by a Fourier series, we further reproduce the 3D droplet shapes on patterned surfaces, where the droplet base lines are provided by simulations or experiments. By detecting and fitting the contact line of the simulated or experimentally captured droplets and matching the dimensions, we are able to apply the contour curve method to calculate the corresponding droplet profile. The results show excellent agreement with the findings of Peng et al.[65] and our previous work[14] (see Fig. S5 and S6 in Supplementary Note 5).

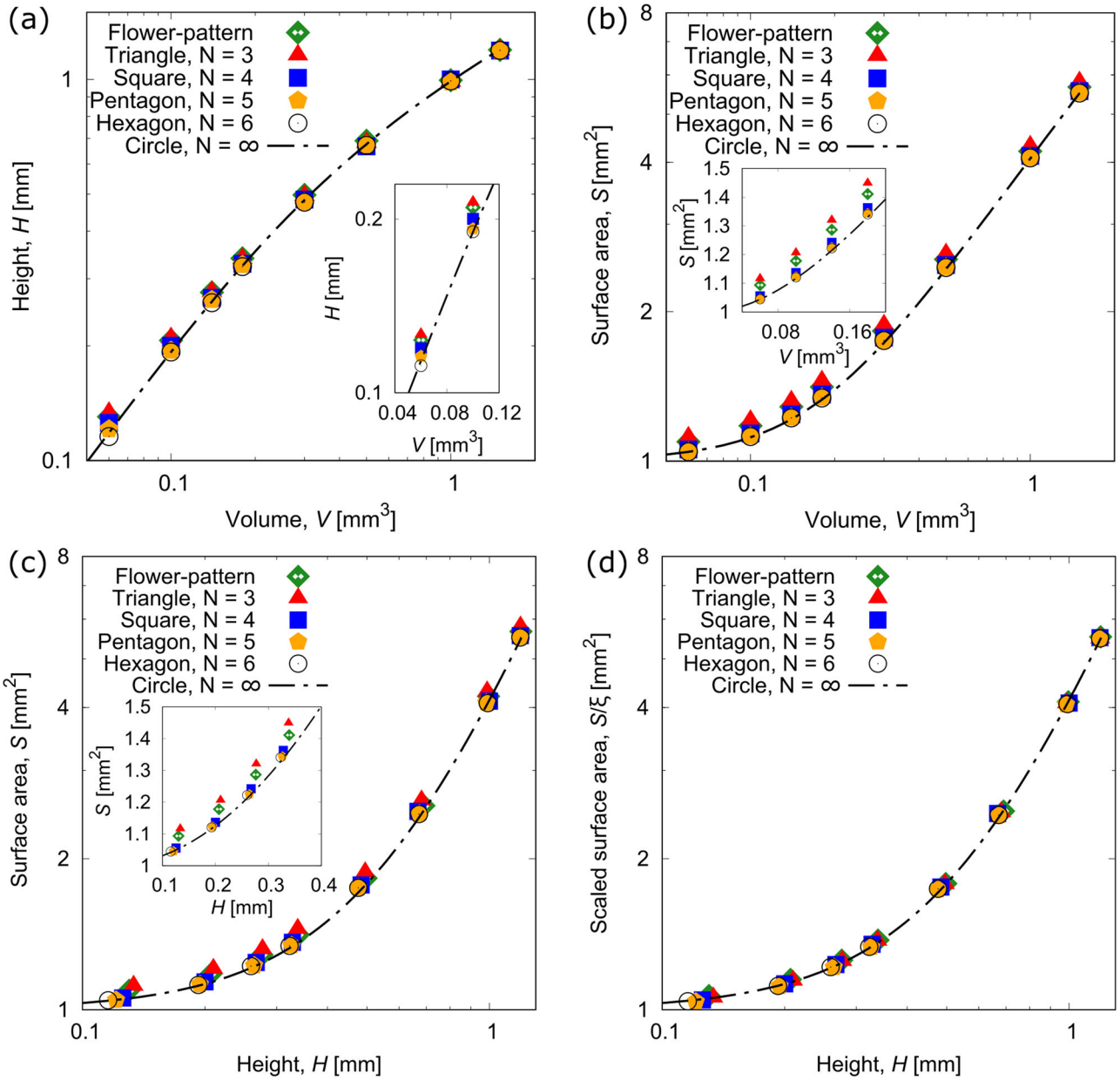

Fig. 6 | Geometric properties of the equilibrated 3D droplets on different patterned substrates. Flower and polygon patterns: symbols; circular pattern: dot dashed lines. Insets provide a zoomed-in view of the respective diagrams. **a** Droplet height H as a function of volume V. **b** Surface area of the droplet cap S vs. volume V. **c** Surface area of the droplet cap S vs. droplet height H. **d** Scaled surface area of the droplet cap S/ξ vs. H. The master curve presented by the dot dashed line follows the expression $S/\xi = S_1 + \pi H^2$, where $S_1 = 1$ mm^2. The distortion coefficient ξ measures the deviation of the droplet shapes from a spherical cap and is as follows: circle-1, triangle-1.056, flower-1.025, square-1.009, pentagon-1.008, hexagon-1.005.

Apart from chemically patterned surfaces, we address irregular droplet contact lines on rough surfaces and attempt to explain the mechanism behind the universal scaling law that describes the contact line roughness[66]. Actually, the behavior of a contact line on a weakly heterogeneous surface is characterized by random fluctuations in interfacial tension. The contact line displacement is assumed to be small and can be analyzed using Fourier components. The liquid-gas interface shape satisfies the Laplace condition and is influenced by the contact line distortion. For an in-depth understanding on the derivation of the universal scaling law that describes the contact line roughness, readers are referred to Supplementary Note 4. Here, we briefly describe the scaling law as follows. Through a detailed analysis of interfacial tension fluctuations, the correction to the capillary energy and the external force causing contact line distortion, it can be observed that the position $\eta(x)$ of the contact line in terms of x resembles the viscous motion of a particle subjected to a random force. This leads to a diffusion-governed behavior[66]:

$$\langle(\eta(x) - \eta(x))^2\rangle = 2D|x|, \tag{5}$$

with D denoting a diffusion coefficient. Eq. (5) identifies a long-range behavior and for a droplet with a macroscopic size L, the fluctuation amplitudes of the contact line follows the scaling law $\eta^2 \sim DL$, i.e., $\eta \sim L^{1/2}$. We reference the works of Decker and Garoff[67], and Bormashenko et al.[68] to substantiate our discussion. These studies illustrate that the values of the exponent for the scaling law are largely universal and highlight that the transition of the exponent is also universal as the roughness size approaches the correlation length of defects. A similar scaling law and relevant investigations have been reported in refs. 69,70, where it was found that the scaling exponents depend on surface properties and the equilibrium contact angle, explaining the experimentally obtained roughness exponents. They

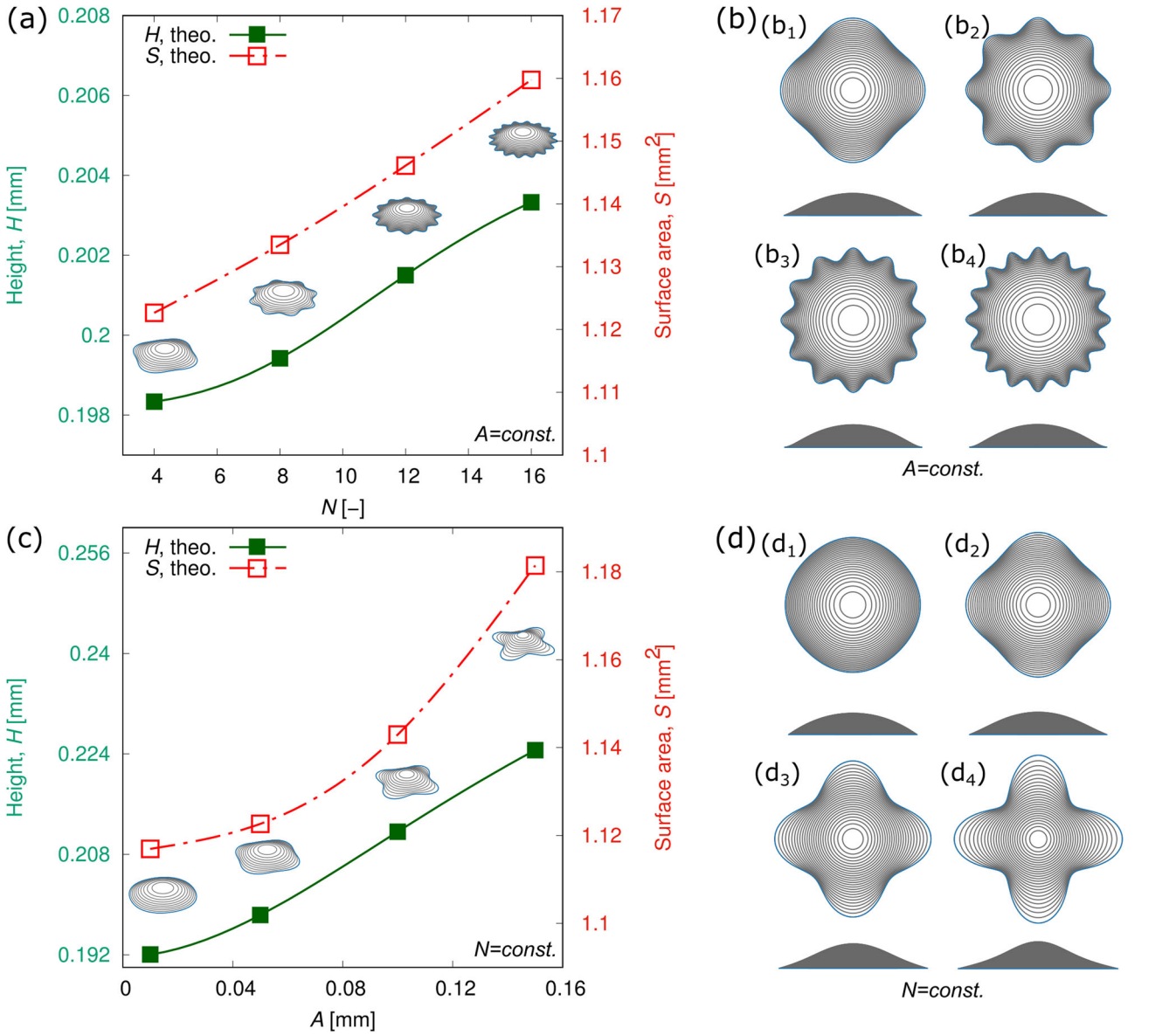

Fig. 7 | Morphological diagram for equilibrium droplets on regular monochromatic patterns via the contour curve method. The base line of the droplet is depicted by $r = A\cos N\theta$. **a** Surface area of the droplet cap S and the droplet height H as a function of N. Here, we keep $A = 0.05$ constant and show the results for $N = 4$, 8, 12, 16. **b** Snapshots for the top and side views of the equilibrated droplets on patterns with different N. **c** S and H as a function of A. We keep $N = 4$ constant and consider the following values of A: 0.01, 0.05, 0.1, 0.15. **d** Snapshots for the top and side views of the equilibrated droplets on patterns with different A.

Table 2 | Calculated distortion coefficient ξ for different A and N as used in Fig. 7

Fixed parameters	Variables	The list of ξ			
$A = 0.05$ mm	N	4	8	12	16
	ξ	1.006	1.015	1.027	1.039
$N = 4$	A (mm)	0.01	0.05	0.1	0.15
	ξ	1.001	1.006	1.024	1.058

showed that defect distribution and shape do not significantly affect the advancing and receding apparent contact angles. Understanding the implications of this universal scaling law will enhance the robustness of our model and provide deeper insights into the wetting behavior of droplets on structured surfaces.

The contour curvature method can be directly applied to droplets on surfaces with 3D physical structures, especially when the 3D surface structures are much smaller than the droplet size and the droplet is in a Cassie state (see Fig. S4a, b in Supplementary Note 4). In the Cassie state, the liquid-gas interface beneath the droplet is almost flat, as utilized in several theoretical works[71,72] and confirmed in many experimental studies[73,74]. However, if the droplet penetrates into the surface structures, the liquid-gas interface at the bottom of the droplet may not be flat, and the present model needs to be extended to consider the liquid volume trapped in the surface structures. A reasonable approach is to estimate the trapped volume based on the surface properties. For instance, for a droplet on a porous surface (e.g., surface porosity P_o, average pore height h_p in the Wenzel state[75], we can modify the droplet volume as $V_m = V - S_1 P_o h_p$ in the contour curve method (see Fig. S4c, d), in Supplementary Note 4). In this case, the functional relationship between droplet height and volume will change, but the new relationship can be easily obtained by shifting the curves from (V, H) to (V_m, H). The calculation procedure of the contour curve method remains the same, except for the modified volume. For more complex wetting states, such as intermediate wetting states, a semi-theoretical model can be applied[76].

Conclusions

In summary, we have proposed a generalized framework to address the morphological properties of droplets with highly irregular footprints on heterogeneous surfaces. Our approach differs from traditional methods of describing droplet wetting morphology via contact angles, such as Young's law and Cassie-Baxter-Wenzel model. Instead, we suggest a contour curve method to characterize the three-dimensional shapes of droplets on heterogeneous surfaces. We have successfully applied the contour curve method to depict the equilibrium shapes of droplets on polygonal patterned and irregular flower-patterned surface; the results are well confirmed by the phase-field simulations. We have also demonstrated the extension of the contour curve method to droplets with arbitrary base lines, even those involving highly irregular patterns. Moreover, we have discussed about the incorporation of the contact angle hysteresis effect into the current contour curve model by describing the droplet baseline via a Fourier series. We have explained the mechanism behind the universal scaling law that describes the contact line roughness for droplets on a weakly heterogeneous surface.

A noteworthy outcome of the present work is the establishment of the correlation between the volume of an equilibrated droplet and its height, irrespective of its shape. This result overcomes the experimental difficulty in measuring the droplet volume on a solid surface, where rapid evaporation and a non-circular footprint complicate the experimental measurement. Based on the current work, the volume of a droplet can be ascertained simply by measuring its height. Moreover, we have proposed a universal functional relationship between the droplet height and the surface area of the droplet cap by introducing the distortion coefficient.

Our investigations pave a way to comprehensively understand the wetting behaviors of droplets with irregular footprints due to surface heterogeneity. This opens up new possibilities for manipulating droplet shapes in various applications, including 3D printing, printed electronics, blood analysis, precise control of evaporation, colloidal patterning. Our approach can be harnessed and extended in situations where external fields such as gravitational, electrical, and magnetic fields are applied.

Methods

Contour curve method

The contour curve method was implemented by using python code which is publicly accessible. Supplementary Information contains more detailed information on the contour curve method.

Numerical model

Phase-field simulations were performed by using volume-conserved Allen-Cahn type formulations, in contrast to the Cahn-Hilliard approach[77]. In this model, we adopt a complex wetting boundary condition considering the Young's contact angle of a droplet on a chemically patterned substrate. In the phase-field model, we use a space and time dependent continuous phase variable $\phi(\mathbf{x}, t)$ to describe the phase state. The states for $\phi = 1$ and 0 correspond to the liquid and gas phases, respectively. When ϕ varies between 0 and 1, it indicates the liquid-gas interface. Specially, we define the interface position at $\phi = 0.5$. The free energy functional of the system in terms of ϕ reads

$$\mathcal{F} = \int_{\Omega} [(1/\epsilon) w(\phi) + f_0(\phi) + \epsilon \gamma_{lg} (\nabla \phi)^2] d\Omega + \int_S f_w(\phi) dS, \quad (6)$$

where Ω and S represent the spatial domain and solid-fluid boundary, respectively. The parameter ϵ is related to the liquid-gas interface width. We introduce an obstacle potential $w(\phi)$, which is expressed as $w(\phi) = (16/\pi^2)\gamma_{lg}\phi(1-\phi)$ for $\phi \in [0, 1]$; and $w(\phi) = \infty$, for $\phi < 0$ or $\phi > 1$. The function $f_0(\phi)$ preserves the volume. The last term $f_w(\phi) = \gamma_{ls} l(\phi) + \gamma_{gs}[1 - l(\phi)]$ is the wall free energy with $l(\phi) = \phi^3(6\phi^2 - 15\phi + 10)$ depicting an interpolation function. The evolution equation for ϕ is obtained through the Allen-Cahn equation $\tau\epsilon\partial_t\phi = -\delta\mathcal{F}/\delta\phi$, which leads to

$$\tau\epsilon\partial_t\phi = -(16/\pi^2)\gamma_{lg}(1-2\phi)/\epsilon + 2\epsilon\gamma_{lg}\Delta\phi - f_0'(\phi) \text{ in } \Omega, \quad (7)$$

$$2\epsilon\gamma_{lg}\nabla\phi \cdot \mathbf{n} = (\gamma_{gs} - \gamma_{ls}) l'(\phi) \text{ on } S. \quad (8)$$

Here, τ is a time relaxation coefficient and $\mathbf{n}$ is the normal vector of the solid-liquid boundary. When the droplet reaches a state of equilibrium, the above boundary condition leads to the Young's law. This model has been validated through theoretical and experimental results in our previous works. Specifically, it has been successful in accurately depicting wetting phenomena across a variety of surfaces. These include homogeneous surfaces[58], chemically patterned substrates[14], funnel-like structures[59], as well as superhydrophobic and superhydrophilic surfaces[78]. The model's broad applicability and precise predictions underscore its potential for further research and practical applications in the field of wetting.

Data availability

The dataset that supports the findings of this study can be found at https://github.com/yanchenwuu/droplet-shape.

Code availability

Source code of the contour curve method has been deposited in GitHub (https://github.com/yanchenwuu/droplet-shape).

Received: 17 August 2024; Accepted: 7 January 2025;
Published online: 24 January 2025

References

1. Young, T. Iii. an essay on the cohesion of fluids. *Philosophical Transactions of the Royal Society of London* 65–87 (1805).
2. Bormashenko, E. Y.*Wetting of real surfaces*, vol. 19 of *De Gruyter Studies in Mathematical Physics* (Walter de Gruyter GmbH and Co KG, Berlin, Germany, 2018).
3. Tadmor, R. Open problems in wetting phenomena: pinning retention forces. *Langmuir* **37**, 6357–6372 (2021).
4. Butt, H.-J. et al. Contact angle hysteresis. *Curr. Opin. Colloid Interf. Sci.* **59**, 101574 (2022).
5. Wang, F. & Nestler, B. Wetting and contact-angle hysteresis: Density asymmetry and van der waals force. *Phys. Rev. Lett.* **132**, 126202 (2024).
6. Zhang, H., Zhang, H., Wang, F. & Nestler, B. Exploration of contact angle hysteresis mechanisms: From microscopic to macroscopic. *J. Chem. Phys.* **161**, 194705 (2024).
7. Aurbach, F., Wang, F. & Nestler, B. Wetting phenomena of droplets and gas bubbles: Contact angle hysteresis based on varying liquid–solid and solid–gas interfacial tensions. *J. Chem. Phys.* **161**, 164708 (2024).
8. Xia, D., Johnson, L. M. & López, G. P. Anisotropic wetting surfaces with one-dimesional and directional structures: fabrication approaches, wetting properties and potential applications. *Adv. Mater.* **24**, 1287–1302 (2012).
9. Lößlein, S. M., Mücklich, F. & Grützmacher, P. G. Topography versus chemistry–how can we control surface wetting? *J. Colloid Interf. Sci.* **609**, 645–656 (2022).
10. Wenzel, R. N. Resistance of solid surfaces to wetting by water. *Ind. Eng. Chem.* **28**, 988–994 (1936).
11. Cassie, A. & Baxter, S. Transactions of the faraday society. *Trans. Faraday Soc.* **40**, 546–551 (1944).
12. Bormashenko, E. Progress in understanding wetting transitions on rough surfaces. *Adv. Colloid Interf. Sci.* **222**, 92–103 (2015).
13. Li, J. et al. Topological liquid diode. *Sci. Adv.* **3**, eaao3530 (2017).
14. Wu, Y. et al. Equilibrium droplet shapes on chemically patterned surfaces: theoretical calculation, phase-field simulation, and experiments. *J. Colloid Interf. Sci.* **606**, 1077–1086 (2022).

15. Wang, F., Wu, Y. & Nestler, B. Wetting effect on patterned substrate. *Adv. Mater.* **35**, 2210745 (2023).
16. Xiang, Y. et al. Superrepellency of underwater hierarchical structures on salvinia leaf. *Proc. Natl. Acad. Sci.* **117**, 2282–2287 (2020).
17. Feng, S. et al. Three-dimensional capillary ratchet-induced liquid directional steering. *Science* **373**, 1344–1348 (2021).
18. Miao, W. et al. Microchannel and nanofiber array morphology enhanced rapid superspreading on animals' corneas. *Adv. Mater.* **33**, 2007152 (2021).
19. Pfeifer, P. & Avnir, D. Chemistry in noninteger dimensions between two and three. i. fractal theory of heterogeneous surfaces. *J. Chem. Phys.* **79**, 3558–3565 (1983).
20. Da Wang, Y. et al. In situ characterization of heterogeneous surface wetting in porous materials. *Adv. Colloid Interf. Sci.* **326**, 103122 (2024).
21. Neogi, S. et al. Tuning thermal transport in ultrathin silicon membranes by surface nanoscale engineering. *ACS Nano* **9**, 3820–3828 (2015).
22. Lu, H., Xu, M., Gong, L., Duan, X. & Chai, J. C. Effects of surface roughness in microchannel with passive heat transfer enhancement structures. *Int. J. Heat. Mass Transf.* **148**, 119070 (2020).
23. Jiang, M. et al. Inhibiting the leidenfrost effect above 1,000 degrees for sustained thermal cooling. *Nature* **601**, 568–572 (2022).
24. Denkov, N., Tcholakova, S., Lesov, I., Cholakova, D. & Smoukov, S. K. Self-shaping of oil droplets via the formation of intermediate rotator phases upon cooling. *Nature* **528**, 392–395 (2015).
25. Haas, P. A., Goldstein, R. E., Smoukov, S. K., Cholakova, D. & Denkov, N. Theory of shape-shifting droplets. *Phys. Rev. Lett.* **118**, 088001 (2017).
26. Shen, Y. et al. From protein building blocks to functional materials. *ACS Nano* **15**, 5819–5837 (2021).
27. George, K. et al. 3d printing of responsive chiral photonic nanostructures. *Proc. Natl. Acad. Sci.* **120**, e2220032120 (2023).
28. Meijer, J. G., Kant, P., Van Buuren, D. & Lohse, D. Thin-film-mediated deformation of droplet during cryopreservation. *Phys. Rev. Lett.* **130**, 214002 (2023).
29. Decuzzi, P., Pasqualini, R., Arap, W. & Ferrari, M. Intravascular delivery of particulate systems: does geometry really matter? *Pharm. Res.* **26**, 235–243 (2009).
30. Pontrelli, G., Carr, E., Tiribocchi, A. & Succi, S. Modeling drug delivery from multiple emulsions. *Phys. Rev. E* **102**, 023114 (2020).
31. Lee, J. K. et al. Spontaneous generation of hydrogen peroxide from aqueous microdroplets. *Proc. Natl. Acad. Sci.* **116**, 19294–19298 (2019).
32. Zhou, G. et al. Controlling the shrinkage of 3d hot spot droplets as a microreactor for quantitative sers detection of anticancer drugs in serum using a handheld raman spectrometer. *Anal. Chem.* **94**, 4831–4840 (2022).
33. Li, Z., Zeng, H. & Zhang, X. Growth rates of hydrogen microbubbles in reacting femtoliter droplets. *Langmuir* **38**, 6638–6646 (2022).
34. Nan, L., Zhang, H., Weitz, D. A. & Shum, H. C. Development and future of droplet microfluidics. *Lab a Chip* **24**, 1135–1153 (2024).
35. Raj, R., Adera, S., Enright, R. & Wang, E. N. High-resolution liquid patterns via three-dimensional droplet shape control. *Nat. Commun.* **5**, 1–8 (2014).
36. Faustini, M. et al. Dynamic shaping of femtoliter dew droplets. *ACS Nano* **12**, 3243–3252 (2018).
37. Lou, J. et al. Polygonal non-wetting droplets on microtextured surfaces. *Nat. Commun.* **13**, 1–9 (2022).
38. Chen, H. et al. Continuous directional water transport on the peristome surface of nepenthes alata. *Nature* **532**, 85–89 (2016).
39. Kreder, M. J., Alvarenga, J., Kim, P. & Aizenberg, J. Design of anti-icing surfaces: smooth, textured or slippery? *Nat. Rev. Mater.* **1**, 1–15 (2016).
40. Guilizzoni, M. Drop shape visualization and contact angle measurement on curved surfaces. *J. Colloid Interf. Sci.* **364**, 230–236 (2011).
41. Ríos-López, I., Karamaoynas, P., Zabulis, X., Kostoglou, M. & Karapantsios, T. D. Image analysis of axisymmetric droplets in wetting experiments: A new tool for the study of 3d droplet geometry and droplet shape reconstruction. *Colloids Surf. A: Physicochem. Eng. Asp.* **553**, 660–671 (2018).
42. Wu, Y., Wang, F., Ma, S., Selzer, M. & Nestler, B. How do chemical patterns affect equilibrium droplet shapes? *Soft Matter* **16**, 6115–6127 (2020).
43. Backholm, M. et al. Toward vanishing droplet friction on repellent surfaces. *Proc. Natl. Acad. Sci.* **121**, e2315214121 (2024).
44. Mcnair, R., Jensen, O. E. & Landel, J. R. Confinement-induced drift in marangoni-driven transport of surfactant: a lagrangian perspective. *J. Fluid Mech.* **986**, A5 (2024).
45. Ishii, T. & Muro, J. The fractal aspects of suminagashi and marbling. *Thin Solid Films* **178**, 109–113 (1989).
46. Mahan, B. Graphical artist https://www.beamahan.com. Pictures taken from flickr (https://www.flickr.com/photos/beamahan) under licence CC BY-NC-ND 2.0 DEED: https://creativecommons.org/licenses/by-nc-nd/2.0/ (2011).
47. Edwards, A. M. et al. Interferometric measurement of co-operative evaporation in 2d droplet arrays. *Appl. Phys. Lett.* **119**, 151601 (2021).
48. Iqtidar, A. et al. Drying dynamics of sessile-droplet arrays. *Phys. Rev. Fluids* **8**, 013602 (2023).
49. Zhang, X. et al. Mixed mode of dissolving immersed nanodroplets at a solid–water interface. *Soft Matter* **11**, 1889–1900 (2015).
50. Brakke, K. A. The surface evolver. *Exp. Math.* **1**, 141–165 (1992).
51. Ueda, E., Geyer, F. L., Nedashkivska, V. & Levkin, P. A. Dropletmicroarray: facile formation of arrays of microdroplets and hydrogel micropads for cell screening applications. *Lab a Chip* **12**, 5218–5224 (2012).
52. Feng, W. et al. Surface patterning via thiol-yne click chemistry: an extremely fast and versatile approach to superhydrophilic-superhydrophobic micropatterns. *Adv. Mater. Interfaces* **1**, 1400269 (2014).
53. Bao, L., Werbiuk, Z., Lohse, D. & Zhang, X. Controlling the growth modes of femtoliter sessile droplets nucleating on chemically patterned surfaces. *J. Phys. Chem. Lett.* **7**, 1055–1059 (2016).
54. Li, H. et al. Droplet precise self-splitting on patterned adhesive surfaces for simultaneous multidetection. *Angew. Chem. Int. Ed.* **59**, 10535–10539 (2020).
55. Gage, M. & Hamilton, R. S. The heat equation shrinking convex plane curves. *J. Differential Geom.* **23**, 69–96 (1986).
56. Chou, K.-S. & Zhu, X.-P.*The curve shortening problem* (Chapman and Hall/CRC, New York, USA, 2001).
57. Wu, Y., Wang, F., Selzer, M. & Nestler, B. Droplets on chemically patterned surface: A local free-energy minima analysis. *Phys. Rev. E* **100**, 041102 (2019).
58. Wu, Y., Wang, F., Selzer, M. & Nestler, B. Investigation of equilibrium droplet shapes on chemically striped patterned surfaces using phase-field method. *Langmuir* **35**, 8500–8516 (2019).
59. Wu, Y., Wang, F., Huang, W., Selzer, M. & Nestler, B. Capillary adsorption of droplets into a funnel-like structure. *Phys. Rev. Fluid* **7**, 054004 (2022).
60. Wu, Y. et al. Digital twin of a droplet microarray platform: Evaporation behavior for multiple droplets on patterned chips for cell culture. *Droplet* **3**, e94 (2024).
61. Arya, P. et al. Wetting behavior of inkjet-printed electronic inks on patterned substrates. *Langmuir* **40**, 5162–5173 (2024).
62. Rahman, M. R. et al. Life and death of a thin liquid film. *Commun. Phys.* **7**, 242 (2024).
63. Wang, F., Zhang, H. & Nestler B. Wetting Phenomena: Line Tension and Gravitational Effect. *Phys. Rev. Lett.* **133**, 246201 (2024).
64. Shanahan, M. E. Disturbed triple line behaviour and its use in surface analysis. *Adv. Colloid Interface Sci.* **39**, 35–59 (1992).

65. Peng, S., Pinchasik, B.-E., Hao, H., Mohwald, H. & Zhang, X. Morphological transformation of surface femtodroplets upon dissolution. *J. Phys. Chem. Lett.* **8**, 584–590 (2017).
66. Joanny, J. & De Gennes, P.-G. A model for contact angle hysteresis. *J. Chem. Phys.* **81**, 552–562 (1984).
67. Decker, E. & Garoff, S. Contact line structure and dynamics on surfaces with contact angle hysteresis. *Langmuir* **13**, 6321–6332 (1997).
68. Bormashenko, E., Musin, A., Whyman, G., Barkay, Z. & Zinigrad, M. On universality of scaling law describing roughness of triple line. *Eur. Phys. J. E* **38**, 2 (2015).
69. Iliev, P., Pesheva, N. & Iliev, S. Roughness of the contact line on random self-affine rough surfaces. *Phys. Rev. E* **98**, 060801 (2018).
70. Iliev, P., Pesheva, N. & Iliev, S. Contact angle hysteresis on nonwetting microstructured surfaces: Effect of randomly distributed pillars or holes. *Phys. Rev. E* **110**, 024801 (2024).
71. Gao, N. & Yan, Y. Modeling superhydrophobic contact angles and wetting transition. *J. Bionic Eng.* **6**, 335–340 (2009).
72. Patankar, N. A. On the modeling of hydrophobic contact angles on rough surfaces. *Langmuir* **19**, 1249–1253 (2003).
73. Rajak, A. & Rühe, J. High hysteresis suspended wetting state: A wetting regime for controlled trapping of drops on micro-trench covered surfaces. *Adv. Mater. Interf.* **9**, 2201018 (2022).
74. Schellenberger, F., Encinas, N., Vollmer, D. & Butt, H.-J. How water advances on superhydrophobic surfaces. *Phys. Rev. Lett.* **116**, 096101 (2016).
75. Berwind, M. et al. Rapidly prototyping biocompatible surfaces with designed wetting properties via photolithography and plasma polymerization. *Microfluidics Nanofluidics* **21**, 1–7 (2017).
76. Nagayama, G. & Zhang, D. Intermediate wetting state at nano/microstructured surfaces. *Soft Matter* **16**, 3514–3521 (2020).
77. Wang, F., Zhang, H., Wu, Y. & Nestler, B. A thermodynamically consistent diffuse interface model for the wetting phenomenon of miscible and immiscible ternary fluids. *J. Fluid Mech.* **970**, A17 (2023).
78. Zhang, H., Wu, Y., Wang, F. & Nestler, B. Effect of wall free energy formulation on the wetting phenomenon: Conservative allen–cahn model. *J. Chem. Phys.* **159**, 164701 (2023).

Acknowledgements

Y.W. thanks funding of the research through the Gottfried-Wilhelm Leibniz prize NE 822/31-1 of the German research foundation (DFG). H.Z. thanks funding of the project KIT Future Field and the German Research Foundation (DFG) in the frame of the Research Training Group 2561: Materials Compounds from Composite Materials for Applications in Extreme Conditions for the funding. F.W. thanks the VirtMat project P09 “Wetting Phenomena” of the Helmholtz association. Impulses for the geometrical arrangements were contributed by funding in the MSE program of the Helmholtz Association (no. 43.31.01). The authors acknowledge support by the state of Baden-Württemberg through bwHPC.

Author contributions

Y.W. and F.W. designed the research. Y.W. contributed to the contour curve concept, F.W. proposed the energy map method, and H.Z. developed the code for the contour curve model. Y.W. and H.Z. performed the research, Y.W., H.Z., and F.W. analyzed the data, and Y.W., H.Z., F.W., and B.N. wrote the paper.

Funding

Open Access funding enabled and organized by Projekt DEAL.

Competing interests

The authors declare no competing interest.

Additional information

Supplementary information The online version contains supplementary material available at https://doi.org/10.1038/s42005-025-01939-z.

Correspondence and requests for materials should be addressed to Fei Wang.

Peer review information *Communications Physics* thanks Zuankai Wang, Edward Bormashenko and the other, anonymous, reviewer(s) for their contribution to the peer review of this work. A peer review file is available.